ACADEMIC PRESS

Available online at www.sciencedirect.com

SCIENCE DIRECT®

Journal of Computational Physics 185 (2003) 532–548

JOURNAL OF COMPUTATIONAL PHYSICS

www.elsevier.com/locate/jcp

A spectral/B-spline method for the Navier–Stokes equations in unbounded domains

L. Dufresne [1], G. Dumas *

Département de Génie Mécanique, Université Laval, Que., Canada G1K 7P4

Received 24 September 2002; accepted 31 December 2002

Abstract

The numerical method presented in this paper aims at solving the incompressible Navier–Stokes equations in unbounded domains. The problem is formulated in cylindrical coordinates and the method is based on a Galerkin approximation scheme that makes use of vector expansions that exactly satisfy the continuity constraint. More specifically, the divergence-free basis vector functions are constructed with Fourier expansions in the θ and z directions while mapped B-splines are used in the semi-infinite radial direction. Special care has been taken to account for the particular analytical behaviors at both end points $r = 0$ and $r \to \infty$. A modal reduction algorithm has also been implemented in the azimuthal direction, allowing for a relaxation of the CFL constraint on the timestep size and a possibly significant reduction of the number of DOF. The time marching is carried out using a mixed quasi-third order scheme. Besides the advantages of a divergence-free formulation and a quasi-spectral convergence, the local character of the B-splines allows for a great flexibility in node positioning while keeping narrow bandwidth matrices. Numerical tests show that the present method compares advantageously with other similar methodologies using purely global expansions.

Keywords: Spectral methods; B-splines; Navier–Stokes equations; Unbounded domains; Divergence-free vector expansions

1. Introduction

In this paper, we present the extension of a mixed B-spline/spectral approach to solve the Navier–Stokes equations in unbounded domains. As an introduction, we briefly cover some preliminary considerations that led to the development of the present method and then give the Navier–Stokes equations with the appropriate set of boundary conditions in cylindrical coordinates. The numerical method is presented in Section 2, including a brief recapitulation of B-spline properties. Application examples for three different flow problems are presented in Section 3. The article concludes by a brief discussion on some performance issues.

* Corresponding author. Fax: +1-418-656-7415.
E-mail address: gdumas@gmc.ulaval.ca (G. Dumas).
[1] Present address: Unite TERM, Département de Mécanique, Université Catholique de Louvain, B-1348 Louvain-la-Neuve, Belgique.

0021-9991/03/$ - see front matter
doi:10.1016/S0021-9991(03)00002-0

1.1. Preliminaries

The numerical solution of unbounded problems requires essentially two levels of approximation [1]. The first one consists in passing from the continuum problem to a discrete set of algebraic equations. The second one requires the proper representation of the boundary conditions.

Let us consider the boundary conditions first and assume that the flow problems of interest here satisfy "physical" periodicity in the longitudinal z direction. We then use a cylindrical coordinate formulation which in turn includes a natural periodic direction in θ. Following this choice, special care must be taken in order to properly account for the regularity conditions at both ends of the radial interval $r = 0$ and $r \to \infty$; the specific behaviors are given below.

As for the discretization of the continuum, we consider Fourier series expansions as the optimal choice for both periodic directions. For the radial coordinate, several types of spectral expansions have already been used for bounded [2–4] and unbounded [1,5,6] intervals, see e.g., Boyd [7] for a more complete review. The bounded methods may be used on a truncated domain but could become expensive for approximating slow decaying functions [1]. The latter unbounded formulations, based on different types of mapped polynomial expansions, are more appropriate for such situations. They also offer some flexibility, through the definition of the mapping function, to adjust the positioning of the computational nodes where they are most needed, but this may come at the expense of having full matrices and loss of spectral convergence (for some possibly high but finite order) as in [8].

This last point led us to undertake the development of the present spectral/B-spline method. The choice of using piecewise polynomials in the mapped radial direction allows for a great flexibility in node positioning while keeping narrow bandwidth matrices. Furthermore, because of their extra smoothness, the local B-spline functions exhibit quasi-spectral convergence properties and are numerically better behaved than some more classical finite element approaches [9,10]. Our choice for B-spline interpolation was also supported, a posteriori, by the publication of an independent but similar methodology developed and used for wall-bounded flow simulations [11,12]. The present work can thus be seen as an extension, for unbounded domains, of the method developed by Loulou et al. [12] for pipe flow simulations.

1.2. Governing equations and boundary conditions

The present numerical method is devised to solve the incompressible, unsteady Navier–Stokes equation

$$\frac{\partial \mathbf{u}}{\partial t} = -\nabla P + \frac{1}{Re}\nabla^2 \mathbf{u} + \mathbf{F} \tag{1}$$

with

$$\nabla \cdot \mathbf{u} = 0. \tag{2}$$

The different terms in (1) and (2) are identified as follows: $\mathbf{u}$ is the velocity vector, $P \equiv p + \frac{1}{2}|\mathbf{u}|^2$ is the total pressure, and $\mathbf{F} \equiv \mathbf{u} \times \boldsymbol{\omega}$ is the nonlinear forcing term which includes the vorticity vector $\boldsymbol{\omega} \equiv \nabla \times \mathbf{u}$. The Reynolds number is defined as $Re \equiv \bar{U}_{\mathrm{ref}}\bar{L}_{\mathrm{ref}}/\bar{\nu}$, where both reference scales $\bar{U}_{\mathrm{ref}}$ and $\bar{L}_{\mathrm{ref}}$ depend on the particular flow problem considered; the overbar notation is used to represent dimensional quantities. Equations (1) and (2) are to be complemented with appropriate initial and boundary conditions. More specifically, for the boundary conditions we have a periodicity condition, aligned with the z coordinate and, perpendicular to it, a decaying condition, respectively, written

$$\mathbf{u}(\mathbf{x}, t) = \mathbf{u}(\mathbf{x} + L_z\hat{\mathbf{e}}_z, t) \text{ and } \lim_{r\to\infty} \mathbf{u}(\mathbf{x}, t) = \mathbf{0}, \tag{3}$$

where L_z is the given periodicity length and $\mathbf{x} = r\hat{\mathbf{e}}_r + \theta\hat{\mathbf{e}}_\theta + z\hat{\mathbf{e}}_z = \{r, \theta, z\}$. In addition, special care must be taken in cylindrical coordinates since the differential operators are singular at both $r = 0$ and $r \to \infty$ [6,7,12,13].

On the longitudinal axis $r = 0$, the analyticity condition requires that the Cartesian components of an arbitrary vector $\mathbf{\Psi}(r, \theta, z) = \sum_{k_\theta, k_z} \widehat{\mathbf{\Psi}}(r) e^{i(k_\theta\theta + k_z z)}$ behave as

$$\lim_{r\to 0}\{\widehat{\psi}_x, \widehat{\psi}_y, \widehat{\psi}_z\} = \mathcal{O}(r^{|k_\theta|+2p}),$$

where p is a non-negative integer and "$\widehat{\ }$" denotes the Fourier transform in θ and z (with corresponding wavenumber k_θ and k_z). For cylindrical vector components, we obtain

$$\widehat{\psi}_r \pm i\widehat{\psi}_\theta = [\widehat{\psi}_x \pm i\widehat{\psi}_y] r^{|k_\theta \pm 1|+2p} \tag{4}$$

with $\widehat{\psi}_z$ remaining unchanged. The complete set of analyticity conditions can thus be written for $r \to 0$ as

$$\begin{aligned}
r[\widehat{\psi}_r + i\widehat{\psi}_\theta] &= \mathcal{O}(r^{k_\theta+2p+2}) \quad \text{for } k_\theta \geqslant 0,\\
r[\widehat{\psi}_r - i\widehat{\psi}_\theta] &= \mathcal{O}(r^{k_\theta+2p}) \quad\ \ \text{for } k_\theta \geqslant 1,\\
r[\widehat{\psi}_r + i\widehat{\psi}_\theta] &= \mathcal{O}(r^{|k_\theta|+2p}) \quad \text{for } k_\theta \leqslant -1,\\
r[\widehat{\psi}_r - i\widehat{\psi}_\theta] &= \mathcal{O}(r^{|k_\theta|+2p+2}) \quad \text{for } k_\theta \leqslant 0,\\
\widehat{\psi}_z &= \mathcal{O}(r^{|k_\theta|+2p}) \quad \text{for } |k_\theta| \geqslant 0
\end{aligned} \tag{5}$$

with $p = 0, 1, 2, 3, \ldots$ At the point $r = 0$, the conditions in (5) simplify to the essential unicity condition $\partial\mathbf{\Psi}(r = 0)/\partial\theta = \mathbf{0}$.

At $r \to \infty$, imposing a decaying condition is somewhat more arbitrary. For example, if the initial condition is related to a vorticity field having a compact support, the flow in the far field could then be considered irrotational since the vorticity would be at most exponentially small there. The same problem could also be formulated in terms of a more general class of flows that would allow algebraically decaying vorticity instead. Let us consider for now a vector field $\widehat{\mathbf{\Psi}}$ that both decays and is harmonic as $r \to \infty$. The Cartesian components must then behave as

$$\lim_{r\to\infty}\{\widehat{\psi}_x, \widehat{\psi}_y, \widehat{\psi}_z\} = \mathcal{O}(r^{-|k_\theta|}), \tag{6}$$

with the additional constraint

$$\lim_{r\to\infty} r^{|k_\theta|}\widehat{\psi}_x = i\,\mathrm{sgn}(k_\theta) \lim_{r\to\infty} r^{|k_\theta|}\widehat{\psi}_y, \tag{7}$$

where $\mathrm{sgn}(k_\theta) \equiv k_\theta/|k_\theta|$ [13]. The two conditions (6) and (7), expressed in terms of the cylindrical vector components, give at once

$$\begin{aligned}
&\lim_{r\to\infty}\{r\widehat{\psi}_r, r\widehat{\psi}_\theta, \widehat{\psi}_z\} = \mathcal{O}(r^{-|k_\theta|}),\\
&\lim_{r\to\infty} r^{|k_\theta|+1}\widehat{\psi}_r = i\,\mathrm{sgn}(k_\theta) \lim_{r\to\infty} r^{|k_\theta|+1}\widehat{\psi}_\theta.
\end{aligned} \tag{8}$$

In the present case, this harmonic decaying behavior is not enforced directly on the velocity vector but rather on a vector $\mathbf{\Psi}$ such that $\mathbf{u} \equiv \nabla \times \mathbf{\Psi}$, giving an algebraically decaying condition on both the velocity and the vorticity fields.

2. Numerical method

The spatial discretization is constructed from a standard Galerkin approximation [7,14] based on the divergence-free approach of Leonard [15]. We follow the Helmholtz–Hodge decomposition formulation [16] where the formal no-through flow condition – or the full no-slip condition used in similar projections for bounded domains [2,12,17,18] – is replaced by an appropriate decaying condition. Thus, by taking the inner product of (1) with a test vector function $\mathbf{\Phi}$ satisfying

$$\nabla \cdot \mathbf{\Phi} = 0 \quad \text{and} \quad \lim_{r\to\infty} \mathbf{\Phi} \cdot \mathbf{n} = 0, \tag{9}$$

we obtain, after integrating by parts the viscous term,

$$\left\langle \mathbf{\Phi}, \frac{\partial \mathbf{u}}{\partial t} \right\rangle = -\frac{1}{Re}\langle \nabla \times \mathbf{\Phi}, \nabla \times \mathbf{u}\rangle + \langle \mathbf{\Phi}, \mathbf{F}\rangle. \tag{10}$$

The inner product is defined here by

$$\langle \mathbf{v}, \mathbf{u}\rangle \equiv \int_{\Omega} \mathbf{v}^* \cdot \mathbf{u}\, \mathrm{d}V, \tag{11}$$

where Ω represents the domain of integration and "*" the complex conjugate. If $\mathbf{u}$ is also made to satisfy the continuity constraint (2) and the homogeneous boundary conditions (3), then Eq. (10) represents the complete statement of the problem to solve.

Now, an approximate solution of (10) is sought in the form of

$$\mathbf{u}(r,\theta,z,t) = \sum_{l}\sum_{m}\sum_{n} \alpha_{lmn}(t)\mathbf{W}_l(r;k_\theta,k_z)\mathrm{e}^{\mathrm{i}k_\theta\theta}\mathrm{e}^{\mathrm{i}k_z z} \tag{12}$$

with

$$k_\theta = m\frac{2\pi}{L_\theta} \text{ and } -N_\theta \leqslant m \leqslant N_\theta,$$

$$k_z = n\frac{2\pi}{L_z} \text{ and } -N_z \leqslant n \leqslant N_z,$$

and $1 \leqslant l \leqslant N_r$. Notice that in the above, the angular periodicity L_θ has been left as an adjustable parameter that may be set to entire fractions of the total arc length 2π.

Now, if the general vector expansion $\mathbf{W}_l$ is divergence-free, then only two independent basis vectors are required to completely define it. These vectors may be associated with a "+" and "−" class [2], and are accordingly identified by the set $\{\mathbf{W}_l^+, \mathbf{W}_l^-\}$. Also, because $\mathbf{u}$ is real, only half of the coefficients $\alpha_{lmn}^{\pm}$ are independent (in m an n), the other half being determined by complex conjugate symmetry. We thus consider for now on that $k_\theta \geqslant 0$.

For the construction of the $\mathbf{W}_l^{\pm}$, we follow Loulou et al. [12], but with a set of different radial basis functions. In the general case, where $k_\theta > 0$ and $k_z \neq 0$, we set

$$\mathbf{W}_l^+ = \widehat{\nabla\times}\begin{Bmatrix} 0 \\ 0 \\ -k_z r G_l \end{Bmatrix} = k_z \begin{Bmatrix} -\mathrm{i}k_\theta G_l \\ (rG_l)' \\ 0 \end{Bmatrix}, \tag{13}$$

$$\mathbf{W}_l^- = \widehat{\nabla\times}\left\{\begin{array}{c} -\mathrm{i}G_l \\ G_l \\ 0 \end{array}\right\} = \left\{\begin{array}{c} -\mathrm{i}k_z G_l \\ k_z G_l \\ G_l' + (1-k_\theta) r^{-1} G_l \end{array}\right\}. \tag{14}$$

The "$\widehat{\nabla\times}$" stands for the Fourier-transformed curl operator and the $G_l(r)$ are real valued functions that form a basis for the radial direction; the variable dependence has been omitted for simplicity. Because (13) and (14) are incomplete when either one or both $k_z = 0$ and $k_\theta = 0$, the following expansions are added: for $k_\theta > 0$ and $k_z = 0$,

$$\mathbf{W}_l^+ = \widehat{\nabla\times}\left\{\begin{array}{c} 0 \\ 0 \\ -rG_l \end{array}\right\} = \left\{\begin{array}{c} -\mathrm{i}k_\theta G_l \\ (rG_l)' \\ 0 \end{array}\right\}, \tag{15}$$

$$\mathbf{W}_l^- = \widehat{\nabla\times}\left\{\begin{array}{c} -\mathrm{i}G_l \\ G_l \\ 0 \end{array}\right\} = \left\{\begin{array}{c} 0 \\ 0 \\ G_l' + (1-k_\theta) r^{-1} G_l \end{array}\right\}, \tag{16}$$

for $k_\theta = 0$ and $k_z \neq 0$,

$$\mathbf{W}_l^+ = \widehat{\nabla\times}\left\{\begin{array}{c} -\mathrm{i}G_l \\ 0 \\ 0 \end{array}\right\} = \left\{\begin{array}{c} 0 \\ k_z G_l \\ 0 \end{array}\right\}, \tag{17}$$

$$\mathbf{W}_l^- = \widehat{\nabla\times}\left\{\begin{array}{c} -\mathrm{i}G_l \\ G_l \\ 0 \end{array}\right\} = \left\{\begin{array}{c} -\mathrm{i}k_z G_l \\ k_z G_l \\ G_l' + r^{-1} G_l \end{array}\right\}, \tag{18}$$

and finally for $k_\theta = 0$ and $k_z = 0$,

$$\mathbf{W}_l^+ = \left\{\begin{array}{c} 0 \\ G_l \\ 0 \end{array}\right\}, \tag{19}$$

$$\mathbf{W}_l^- = \left\{\begin{array}{c} 0 \\ 0 \\ r^{-1} G_l \end{array}\right\}. \tag{20}$$

We now replace (12) in (10) with the test vector functions defined as $\mathbf{\Phi} \equiv \mathbf{W}_{l'}^{\pm} \mathrm{e}^{\mathrm{i}k'_\theta \theta} \mathrm{e}^{\mathrm{i}k'_z z}$ and thus obtain, for each independent modal pair k_θ, k_z, a set of ODEs symbolically written as

$$\begin{aligned} \mathsf{A}_+^+ \dot{\alpha}^+ + \mathsf{A}_+^- \dot{\alpha}^- &= \mathsf{B}_+^+ \alpha^+ + \mathsf{B}_+^- \alpha^- + \mathsf{F}^+, \\ \mathsf{A}_-^- \dot{\alpha}^- + \mathsf{A}_-^+ \dot{\alpha}^+ &= \mathsf{B}_-^- \alpha^- + \mathsf{B}_-^+ \alpha^+ + \mathsf{F}^-. \end{aligned} \tag{21}$$

The $\dot{\alpha}^\pm$ represents the time derivative of $\alpha^\pm$ and the various indices as well as the summation in l are here implicitly assumed. The components of the radially coupled inertia A and viscous B matrices are, respectively, given by

$$[\mathsf{A}_\delta^\gamma]_{l'l} = \int_0^\infty (\mathbf{W}_{l'}^\delta)^* \cdot (\mathbf{W}_l^\gamma) r \, \mathrm{d}r \quad \text{and} \tag{22}$$

$$[\mathsf{B}^{\gamma}_{\delta}]_{l'l} = -\frac{1}{Re}\int_0^{\infty} (\widehat{\nabla\times\mathbf{W}}^{\delta}_{l'})^{*}\cdot(\widehat{\nabla\times\mathbf{W}}^{\gamma}_{l}) r\,\mathrm{d}r \tag{23}$$

with δ and γ symbolizing alternatively both the "+" and "−" classes. As for the nonlinear term

$$\{\mathsf{F}^{\gamma}\}_{l'} = \frac{1}{L_\theta L_z}\int\int\int \mathbf{W}^{\gamma *}_{l'm'n'} \mathrm{e}^{-\mathrm{i}k'_\theta\theta}\mathrm{e}^{-\mathrm{i}k'_z z}\cdot\left[\sum_{l}\sum_{m,n}\alpha^{\pm}_{lmn}\mathbf{W}^{\pm}_{lmn}\mathrm{e}^{\mathrm{i}k_\theta\theta}\mathrm{e}^{\mathrm{i}k_z z}\times\nabla \times\left(\sum_{l_*}\sum_{m_*,n_*}\alpha^{\pm}_{l_*m_*n_*}\mathbf{W}^{\pm}_{l_*m_*n_*}\mathrm{e}^{\mathrm{i}k_{\theta *}\theta}\mathrm{e}^{\mathrm{i}k_{z*}z}\right)\right] r\,\mathrm{d}r\,\mathrm{d}\theta\,\mathrm{d}z, \tag{24}$$

it is evaluated using a de-aliased pseudospectral procedure in the Fourier directions [7,14] and convolution sums in the radial coefficient space [11–13]. Finally, the time marching of (21) is carried out using the mixed implicit/explicit, quasi-third order scheme proposed by Spalart et al. [19]; the marginal stability curve of the scheme is shown in Fig. 1.

2.1. B-spline functions

The radial dependency of the vector functions introduced above is now addressed. More specifically, the radial basis functions G_l are constructed from mapped B-splines, and are at the heart of the present spatial discretization. We therefore begin by considering the mapping function and then cover some of the basic properties of B-spline functions.

The unbounded radial domain $r \in [0,\infty[$ is mapped into the bounded interval $\eta \in [0,1]$ using as simple a relation as possible, i.e., in the present case the algebraic mapping

$$\eta = \frac{r}{r+L}, \tag{25}$$

where L is an adjustable scaling parameter; see [1] for further details. As a consequence of (25), the generic decaying behavior

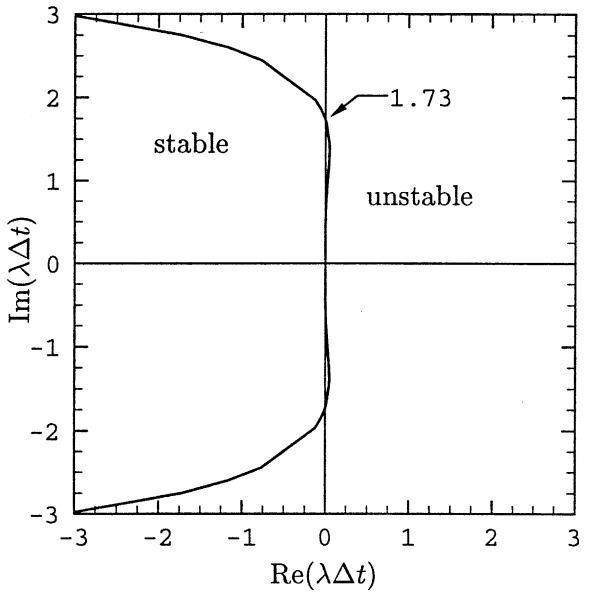

Fig. 1. Marginal stability curve for the time marching scheme, proposed by Spalart et al. [19], for the linear equation $\mathrm{d}u/\mathrm{d}t = \lambda u$. The scheme is stable in the region at the left of the curve.

$$\lim_{r\to\infty} g(r) = \mathcal{O}(r^{-k_\theta}), \tag{26}$$

transforms to

$$\lim_{\eta\to 1} g(r(\eta)) = \mathcal{O}((1-\eta)^{k_\theta}), \tag{27}$$

i.e., a k_θ-fold zero condition at $\eta = 1$ – the function $g(r(\eta))$ and its $k_\theta - 1$ first derivatives are zero at that point. From this result, the decaying conditions expressed in (8) can be enforced on (13)–(20) in a straightforward manner. As for the regularity conditions (5), they remain essentially unchanged since $\eta \sim r/L$ as $r \to 0$. Both sets of regularity/boundary conditions are thus representable by polynomial functions of order k_θ or less.

Let us now formally define our basis functions on the mapped domain such that

$$G_l(r(\eta)) \equiv B_l(\eta), \tag{28}$$

and where B_l is a B-spline of adjustable order k [20]. B-splines of order k, or degree $k-1$, can be evaluated using the recurrence relation

$$B_l^{(k)}(\eta) = \frac{\eta - t_l}{t_{l+k-1} - t_l} B_l^{(k-1)}(\eta) + \frac{t_{l+k} - \eta}{t_{l+k} - t_{l+1}} B_{l+1}^{(k-1)}(\eta) \tag{29}$$

with first order B-splines being simply defined as unitary "top hat" functions, viz.

$$B_l^{(1)}(\eta) = \begin{cases} 1, & t_l \leqslant \eta < t_{l+1}, \\ 0, & \text{otherwise.} \end{cases} \tag{30}$$

Following de Boor's notation [20], the set $\{t_l\}$ defines here the knots on which rests the radial discretization. B-splines are C^{k-2} continuous piecewise polynomials with a compact support defined such that

$$B_l(\eta) = 0 \quad \text{for } \eta \notin [t_l, t_{l+k}]. \tag{31}$$

Furthermore, from the above definitions it may also be shown that

$$B_{l'}(\eta) B_l(\eta) \begin{cases} \neq 0, & l' - k + 1 \leqslant l \leqslant l' + k - 1, \\ = 0, & \text{otherwise.} \end{cases} \tag{32}$$

The nonzero values in both set of matrices (22) and (23) are thus confined to a narrow bandwidth of $2k-1$ and the convolution sums in (24) can in turn be evaluated in $\mathcal{O}(N_r k^2)$ operations instead of $\mathcal{O}(N_r^2)$. An example of a simple, but complete, fourth order B-spline discretization is shown in Fig. 2.

The particular basis functions $G_5(r)$, associated to the spline $B_5(\eta)$ of Fig. 2, are additionally illustrated in Fig. 3 for different values of the mapping parameter L. Note finally that the regularity/boundary conditions are technically imposed by properly constraining the $k-1$ coefficients $\alpha_{lmn}^{\pm}$ attached to each one of the two end points $\eta = 0$ and 1.

3. Examples

The numerical method presented in the previous section has been the object of an extensive validation [13]. In this section, we present three examples of applications related to the linear stability and early stage nonlinear dynamics of some particular vortex flows.

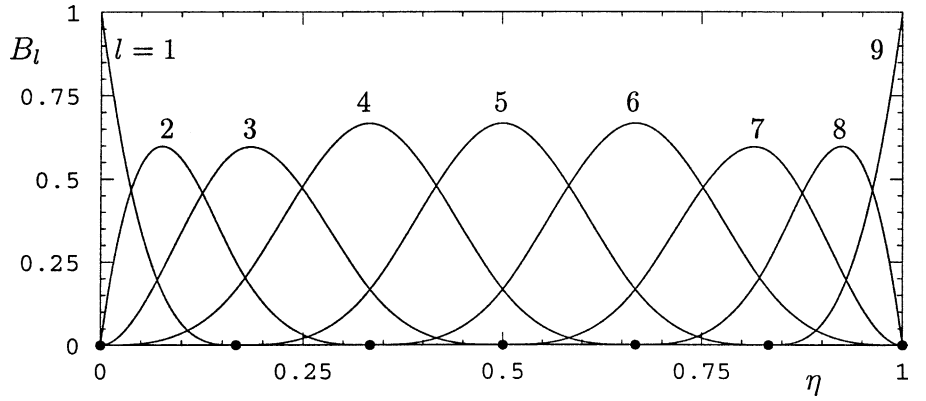

Fig. 2. A simple but complete set of 9 cubic ($k = 4$) B-splines. The knots t_l are identified by the "•" symbols, uniformly distributed in this particular example.

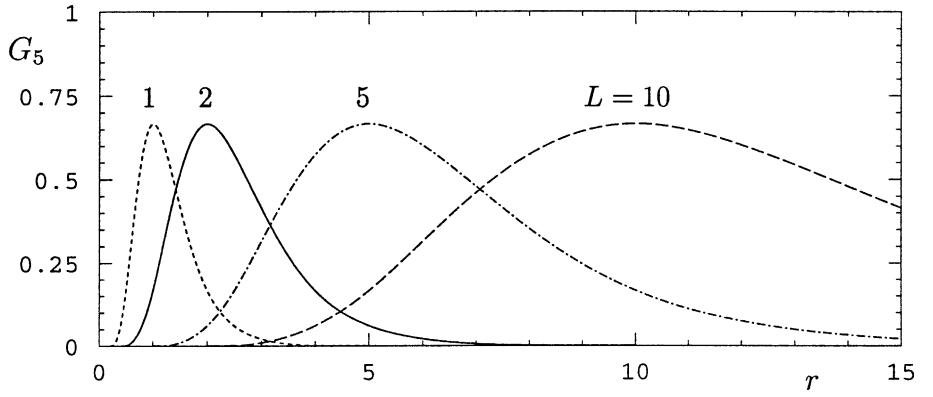

Fig. 3. The basis functions G_5 that correspond to B_5 of Fig. 2 for the different mapping parameter values $L = 1, 2, 5$, and 10.

3.1. Linear stability of a trailing line vortex

The trailing line or Batchelor q-vortex flow is composed of a Gaussian (Lamb–Oseen) vortex to which is superposed an axial jet-like flow [21], as shown in the schematic representation of Fig. 4. The base flow field is written

$$\mathbf{U}(r) = 0\hat{\mathbf{e}}_r + \frac{q}{r}(1 - \mathrm{e}^{-r^2})\hat{\mathbf{e}}_\theta + h\mathrm{e}^{-\beta r^2}\hat{\mathbf{e}}_z, \tag{33}$$

where q scales the swirl intensity, h the centerline axial velocity, and β the relative radial extent of the axial flow with respect to the vortex core size. The dimensional length and velocity scales are chosen as the vortex core size radius $\bar{a}$ and the fraction $1/h$ of the centerline axial velocity $\bar{U}_z(r = 0)$ yielding the Reynolds number $Re \equiv \bar{U}_z\bar{a}/h\bar{\nu}$.

The linear stability of (33) is formulated through a normal mode decomposition [22] such that $\mathbf{u} = \mathbf{U} + \mathbf{u}'$ and

$$\mathbf{u}' = \widehat{\mathbf{u}}(r)\mathrm{e}^{\mathrm{i}(k_\theta\theta + k_z z)}\mathrm{e}^{\lambda t} + \text{c.c.},$$

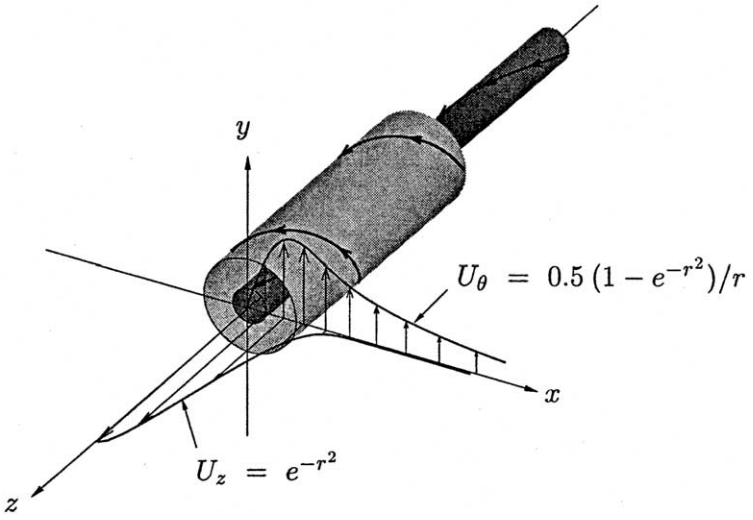

Fig. 4. Perspective view of a q-vortex having parameter values of $q = 0.5$ and $h = \beta = 1$. The vortex tube is represented by the two iso-surfaces of longitudinal vorticity, $\omega_z = 0.8$ (inner surface) and $\omega_z = 0.2$ (outer surface). The spiral lines represent fluid particle trajectories on each one of these surfaces.

where "c.c." stands here for the complex conjugate. After replacing **u** in (10) and linearizing for the perturbation **u**′, one ends up, for each modal pair (k_θ,k_z), with a generalized eigenvalue problem

$$\lambda \mathsf{A}\alpha = [\mathsf{B} - \mathsf{O}]\alpha, \tag{34}$$

where O is the linearized transport matrix. The complex valued $\lambda(= \lambda_r + \mathrm{i}\lambda_i)$ are then obtained using a QZ-algorithm [23].

In Table 1, we show the results for the most unstable eigenmode for $k_\theta = 1$, $k_z = 0.05$, with $q = 0.5$ and $h = \beta = 1$, at $Re = 25$. Here, N_r^* is the number of "free" B-splines after imposing the boundary conditions, the equivalent of the number of global expansion radial modes. The benchmark values computed by Matsushima and Marcus [6] and Mayer and Powell [3] are also given for comparison. In the first case, the

Table 1
The most unstable eigenvalue for $k_\theta = 1$, $k_z = 0.05$, with $q = 0.5$, $h = \beta = 1$, and $Re = 25$

N_r^*	$\lambda \times 10^4$
10	9.936010736 + i22.40212147
20	9.885122155 + i22.38851112
30	9.885158802 + i22.38705093
40	9.885164246 + i22.38703955
50	9.885164396 + i22.38703911
60	9.885164411 + i22.38703907
70	9.885164411 + i22.38703907
Ref. [6][a]	9.8851644 + i22.387039
Ref. [3][b]	9.8851643 + i22.387039

The results are obtained with uniformly distributed B-splines (in η) with $k = 6$ and $L = 11$.
[a] Rational Legendre functions: $N_r^* = 60$ and $L = 12$.
[b] Chebyshev polynomials; $N_r^* = 300$ and $R_o = 200$.

radial discretization was done with rational Legendre functions on an unbounded domain having similar boundary conditions as the ones used here. In the second case, Chebyshev polynomials were used in combination with a no-slip condition imposed at a large but finite outer radius R_o. The present B-spline values are seen to compare advantageously with both global method results.

As another example of application, we computed the neutrally stable ($\lambda_r = 0$) asymmetric oscillations of an inviscid columnar vortex for different values of the defining parameters q, h, and β, all for $k_\theta = 1$. The results are shown in Table 2 and were obtained with $N_r^* = 20$ (uniformly distributed) and $k = 5$. All four digits shown are significant; computations with $N_r^* = 40$ were also carried out to check the accuracy. The mapping parameter L was chosen, for each case, in order to minimize the difference between the results at the two levels of discretization. This procedure is somewhat equivalent to the choice of optimal mapping parameter used in [6]. As another comparison point, we include the values obtained by the long-wavelength asymptotic analysis of Moore and Saffman [24] (cited from [6]) and given by

$$\frac{\lambda_i}{q} = -\frac{k_z^2}{2}\left[\ln k_z + \frac{1}{2}(\gamma - \ln 2) + \frac{h^2}{2q^2\beta} + \frac{hk_z}{q\beta(1+\beta)}\right]\frac{1}{1 + hk_z/q\beta}, \tag{35}$$

where $\gamma = 0.57721566\ldots$ (Euler's constant). Both sets of numerical results are seen to be identical and are in close agreement with the theoretical values, in particular for small k_z (long wavelengths). The present mapped B-spline approach is again seen to compare advantageously with the reference data.

3.2. Emergence of a triangular vortex

Some particular two-dimensional multipole vortices have been studied both experimentally and numerically [25–27]. Among the different compound vortex structures observed is the so called "triangular

Table 2
The positive valued λ_i, of the neutrally stable inviscid columnar vortex; for all cases $k_\theta = 1$

No.	k_z	h/q	β	L	$\lambda_i/q \times 10^4$		
					B-spline	Ref. [6][a]	Eq. (35)
1	0.4	0.0	–	4	897.0	897.0	779.0
2	0.2	0.0	–	5	344.1	344.1	333.5
3	0.1	0.0	–	7	118.9	118.9	118.0
4	0.05	0.0	–	10	38.24	38.24	38.17
5	0.025	0.0	–	15	11.71	11.71	11.71
6	0.025	2.0	1.0	11	5.127	5.127	5.125
7	0.025	1.0	1.0	11	9.865	9.865	9.861
8	0.025	−1.0	1.0	11	10.45	10.45	10.45
9	0.025	−2.0	1.0	11	5.832	5.832	5.828
10	0.025	2.0	0.5	–	*	*	*
11	0.025	1.0	0.5	11	8.081	8.081	8.076
12	0.025	−1.0	0.5	11	9.150	9.150	9.145
13	0.025	−2.0	0.5	-	*	*	*
14	0.025	2.0	2.0	8	8.353	8.353	8.349
15	0.025	1.0	2.0	10	10.78	10.78	10.78
16	0.025	−1.0	2.0	10	11.08	11.08	11.08
17	0.025	−2.0	2.0	9	8.835	8.835	8.831

The present B-spline results were obtained with $N_r^* = 20$ and $k = 5$. For comparison, we include the equivalent results of Ref. [6] and the asymptotic values from Eq. (35).

[a] $N_r^* = 59$; from Table V in the reference.

* No positive values were found.

vortex": a triangular shape vortex core surrounded by three vortex satellites of opposite sign vorticity. This particular structure can be seen to emerge from a mode-3 instability of the base flow vorticity profile

$$\Omega_z(r;\alpha) = (\frac{1}{2}\alpha r^{\alpha} - 1)\mathrm{e}^{-r^{\alpha}} \tag{36}$$

with corresponding velocity $U_\theta(r;\alpha) = -r\mathrm{e}^{-r^{\alpha}}/2$, and where $\alpha > 0$. A few examples of the family of profiles (36) are shown in Fig. 5 for different values of the parameter α. The reference time and length scales used for normalization are, respectively, the inverse of the core center vorticity $\bar{\Omega}_0^{-1}$ (with $\bar{\Omega}_0 \equiv \bar{\Omega}_z(\bar{r} = 0)$) and the velocity profiles "crossing point" $\bar{R}_c$. The velocity scale directly follows as $\bar{\Omega}_0\bar{R}_c$ which in turn gives the Reynolds number $Re \equiv \bar{\Omega}_0\bar{R}_c^2/\bar{\nu}$.

We simulated the nonlinear evolution of the $\alpha = 7$ profile to which was added a low-amplitude white-noise perturbation. The Reynolds number was set to $Re = 10^4$ and the simulation was carried out with $N_r = 95$, $k = 5$, $L = 2$. The temporal evolution of the vortex is shown in Fig. 6. The most unstable mode-3 is closely followed by the other low-order modes which lead to the eventual break-up of the triangular vortex. The linear phase growth rates are given in Table 3, and are compared with their corresponding quasi-inviscid values (the B-spline values were obtained with $Re = 10^8$). These results are in very good agreement with both the experimental observations and the numerical simulations found in [26].

The timestep size Δt used to carry out our simulation was set to satisfy the CFL condition

$$\frac{2}{3}\pi\Delta t \max\left[\frac{|u_r|}{\Delta r} + \frac{|u_\theta|}{r\Delta\theta} + \frac{|u_z|}{\Delta z}\right] = 1.7,$$

where the "max" is taken on the whole computational domain. In order to alleviate the possible over resolution associated with a uniform Fourier truncation, i.e., $N_\theta = \text{const.}$ and $\Delta\theta = (3/2)\pi/N_\theta$ so that $r\Delta\theta \to 0$ as $r \to 0$, a modal reduction procedure [11–13,28] was implemented. Here, we used four different radial zones with truncation levels: from inside out $N_\theta = \{6, 20, 42, 84\}$. The effective pseudo-computational grid is show in Fig. 7, superposed to the $t = 50$ solution. With this discretization, Δt varied between ≈ 0.01 and 0.04. The modal reduction technique may also possibly leads to a significant reduction of the number of DOF. In the present example, we have a 28% reduction compared to a single zone with $N_\theta = 84$.

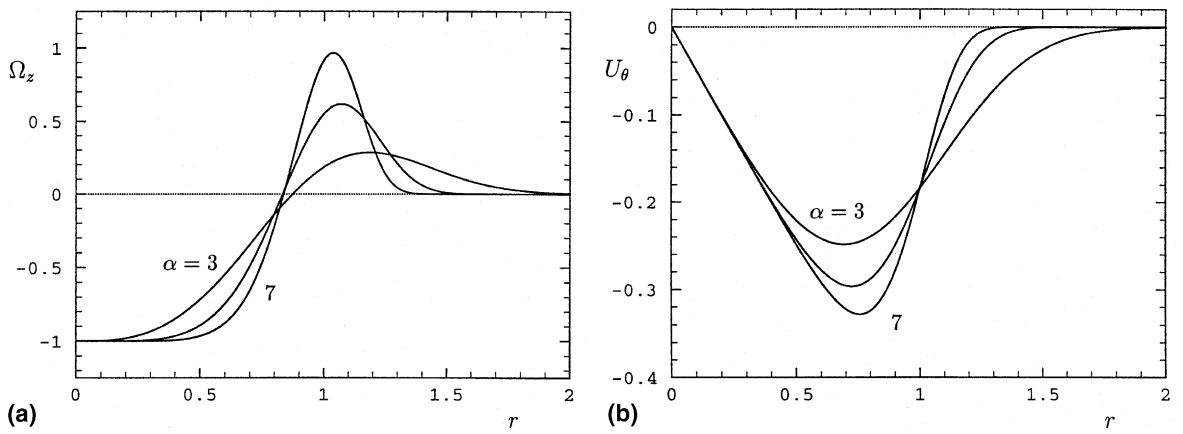

Fig. 5. Different profiles of vorticity (a) and velocity (b) corresponding to (36). The curves are plotted for $\alpha = 3$, 5, and 7.

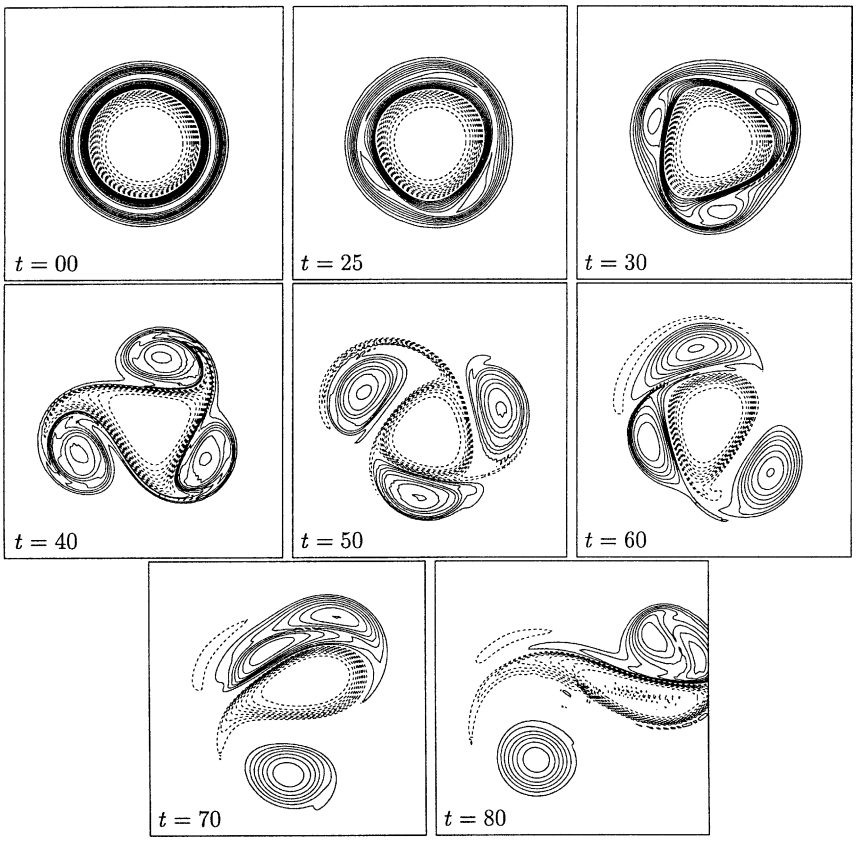

Fig. 6. Emergence of a triangular vortex from an initial white noise perturbation ($\alpha = 7$ and $Re = 10^4$). The vorticity contour values range from -1 to $+1$ with increments of 0.1; dash lines are for negative values and the zero contour is skipped. The presence of various low-order mode instabilities leads to the break-up of the triangular (mode-3) symmetry and the eventual pairing of some of the satellites.

Table 3
Most unstable quasi-inviscid perturbation growth rate values for $k_0 = 2$, 3, and 4, with $\alpha = 7$, along with the $Re = 10^4$ values

	Inviscid			$Re = 10^4$	
	Ref. [26][a]	NM[b]	DNS[c]	NM[b]	DNS[c]
$k_0 = 2$	0.220	0.220	0.21	0.21605	0.22
3	0.242	0.240	0.24	0.23461	0.234
4	0.197	0.194	0.19	0.18724	0.187

[a] Data interpolated graphically from Fig. 7 in [26].
[b] Present B-splines: Normal Mode analysis.
[c] Present B-splines: Navier–Stokes simulation.

To verify the level of spatial resolution used, we checked the 2-D kinetic energy decay

$$\frac{\mathrm{d}E}{\mathrm{d}t} = -2Re^{-1}\mathscr{E}, \tag{37}$$

where we have the total energy $E \equiv \frac{1}{2}\int_\Omega |\mathbf{u}|^2 \,\mathrm{d}V$ and the total entrophy $\mathscr{E} \equiv \frac{1}{2}\int_\Omega |\boldsymbol{\omega}|^2 \,\mathrm{d}V$. It has been confirmed that (37) was satisfied to at least six digit accuracy up to about $t = 60$. As the vortex structures move

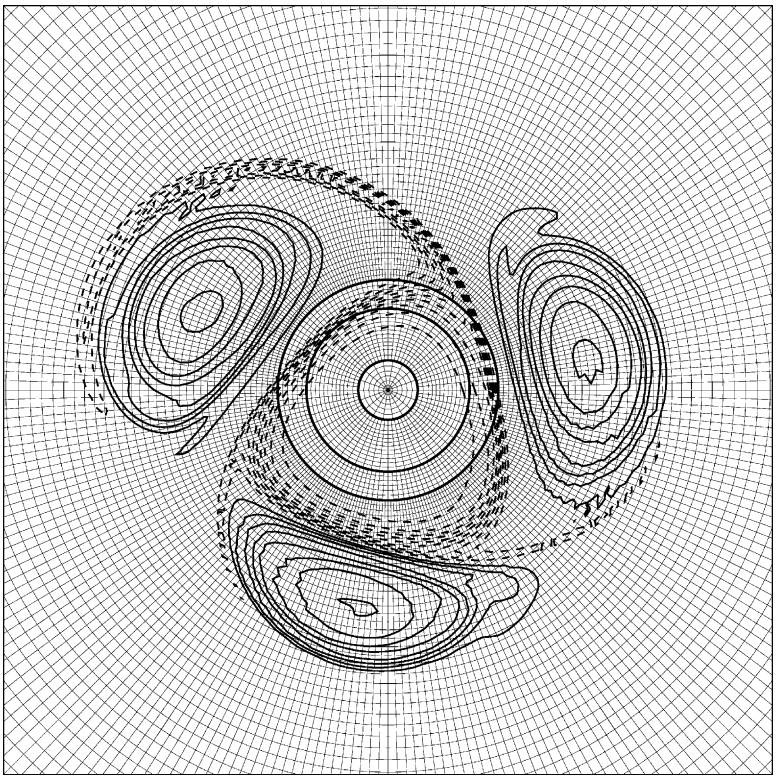

Fig. 7. A partial view of the pseudo-collocation grid used to evaluate the CFL criterion of the computation shown in Fig. 6. Note the variation of modal resolution, from the center out $N_\theta = \{6, 20, 42, 84\}$. The $t = 50$ solution is also shown in background for reference.

away from the domain center, the effective resolution obviously lowers and numerical error increases, to become apparent at $t = 80$ in Fig. 6. This shows the limitations of the present method for the simulation of flow problems that strongly depart from any polar or axial symmetry.

3.3. Long-wave instability of a vortex pair

The third and last example relates to the development of a long-wave instability on a pair of counter-rotating vortices, also known as a Crow instability [29]. The initial base flow is first defined in terms of two counter-rotating Gaussian vortices such that

$$\Omega_z = G(x - \frac{1}{2}, y; a) - G(x + \frac{1}{2}, y; a), \tag{38}$$

where

$$G(x, y; a) \equiv \frac{2}{a^2} \exp\left(- \frac{x^2 + y^2}{a^2} \right). \tag{39}$$

The parameter a is the characteristic length associated with the vortex core size. It is defined such that 63.2% of the total circulation is included within a radius $r = a$ around the vortex center. For this

problem, the dimensional length and velocity scales are, respectively, chosen as the vortices centerline inner spacing $\bar{L}_{\text{ref}} = \bar{b}$ and the self-induced velocity $\bar{U}_{\text{ref}} = \bar{\Gamma}/(2\pi\bar{b})$ (in the limit $a \to 0$). Following these definitions, the nondimensional circulation Γ of a single vortex is thus $\Gamma = 2\pi$, and the Reynolds number is $Re \equiv \bar{\Gamma}/2\pi$. Finally, for all the results shown below, we used the numerical values $a = 0.2$ and $Re = 2600$.

The base flow in (38) does not represent an equilibrium solution. Each one of the two vortices will deform under the presence of a straining field induced by the adjacent vortex. A near equilibrium solution was thus obtained after letting the pair interact for 1 time unit (the straining field time scale). To maintain the vortex pair centered in the computational domain, a background upward velocity $U_{\text{bg}} = 0.95$ was furthermore added. The vortex pairs, before and after deformation, are shown in Fig. 8. The strained vortex pair was obtained by a 2-D computation with $N_r = 89$, $k = 4$, $L = 2$, and a multizone truncation $N_\theta = \{06, 18, 33, 65, 48\}$. The time marching was carried out with the criterion CFL $= 1.7$, which in turn led to $\Delta t \approx 1.5$–3.5×10^{-3}. In this case, because of the important velocities present between the two vortices (i.e., in the center of the computational domain), the modal reduction procedure is critical in order to keep the timestep size at an acceptable value.

The initial condition for the computation of the instability was chosen as the 3-D extension of the solution shown in Fig. 8(b), with a periodicity length of $L_z = 6.5$, corresponding to the most unstable long-wavelength of an equivalent Rankine vortex [30]. A low amplitude, long-wavelength perturbation was then added to this new initial base flow field. The time evolution of the vortex pair is shown in Fig. 9; the computation was carried out with a longitudinal truncation $N_z = 16$. The results are in good qualitative agreement with both the experimental results of Leweke and Williamson [30] and the numerical ones of Laporte and Corjon [31].

4. Discussion

The various numerical tests carried out [13] showed that the present approach, using of local mapped B-splines (in combination with spectral expansions), offers an advantageous alternative to purely global functions [3,6] in the semi-infinite radial direction.

As for the global performance of such mixed spectral/B-spline approaches to solve the complete 3-D unsteady Navier–Stokes equations, Loulou et al. [12], with a very similar method to this one, reported comparable performances between their spectral/B-spline code and the mixing layer code (using Jacobi polynomials instead of B-splines) of Spalart et al. [19]. It must nevertheless be noted that the cost of the computation of the nonlinear term, in the present formulation, can become quite expensive.

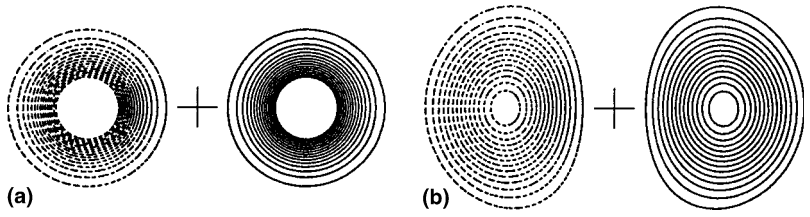

Fig. 8. A 2-D section view of the vorticity distribution of the pair of Gaussian vortices, with $a = 0.2$, is shown in (a). In (b), the resulting strained vortices after an evolution of 1 time unit in a reference frame moving downward at a nondimensional velocity of 0.95. Contours are for $\omega_z = -30$ to 30 with $\Delta\omega_z = 1$; the zero contour is skipped and dash lines are for negative values. The light cross indicates the center of the computational domain.

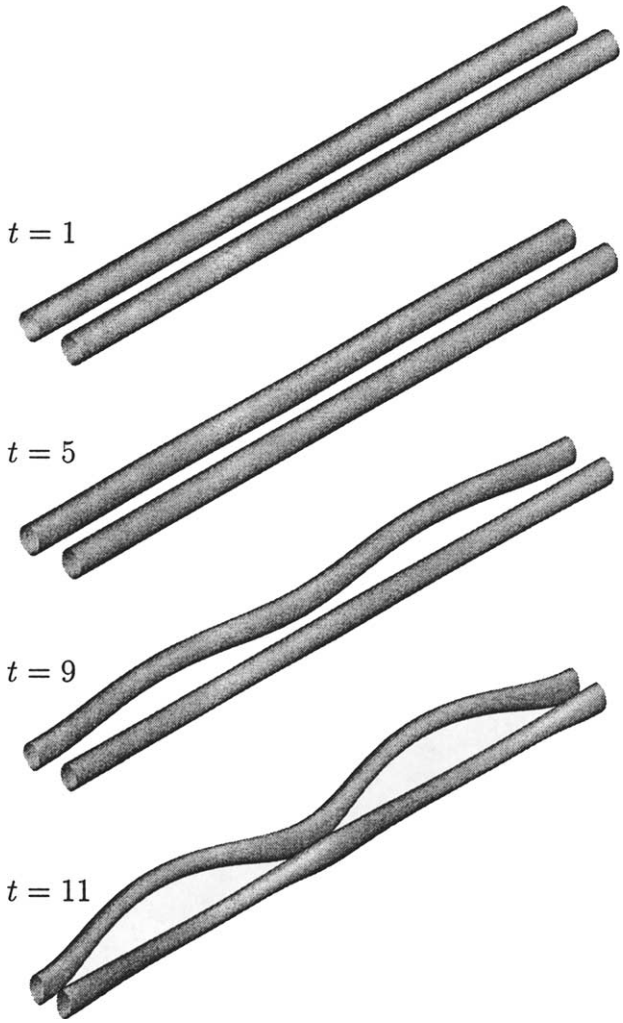

Fig. 9. Time evolution of the long-wavelength instability on the pair of counter-rotating vortices; the different times are shown on the figure. The vortex tubes are represented, over two periodicity lengths, by iso-surfaces of $|\omega| = 10$, and are viewed with a perspective angle aligned with one of the two planes of instability such that the right vortex appears almost undeformed.

Kravchenko et al. [32] have reported figures in the range of 50% of the total CPU time for the computation of that term. Values of 85% have been reported by Loulou et al. [12], and according to the level of generality with which is implemented the modal reduction algorithm, this value can even rise up to 90% [13].

Such considerations have recently led to the development of B-spline collocation approaches [33,34] as a possible alternative. On the other hand, collocation methodology does not offer the advantages of a divergence-free formulation – which requires the projection onto an appropriate functional space and thus the use of basis functions – and it remains unclear to these authors which one is the most performing method. Let us finally mention that a more complete discussion regarding the resolution properties of local interpolation functions, including B-splines, can be found in the recent article by Kwok et al. [35].

Acknowledgements

The financial support of NSERC Canada, through its research grant (G.D.) and scholarship (L.D.) programs, is gratefully acknowledged by the authors. Also, special thanks to R. Brochu for providing us with Fig. 4.

References

[1] C.E. Grosch, S.A. Orszag, Numerical solution of problems in unbounded regions: coordinate transforms, J. Comp. Phys. 25 (1977) 273–296.
[2] A. Leonard, A. Wray, A new numerical method for the simulation of 3-D flow in a pipe, in: Proc. 8th Int. Conf. Num. Meth. Fluid Dyn., Aachen, 1982.
[3] E.W. Mayer, K.G. Powell, Viscous and inviscid instabilities of a trailing vortex, J. Fluid Mech. 245 (1992) 91–114.
[4] T. Matsushima, P.S. Marcus, A spectral method for polar coordinates, J. Comp. Phys. 120 (1995) 365–374.
[5] X. Shi, L. Wu, A spectral method for unbounded flow in a cylindrical coordinate system, in: ESAIM: Proc. (2nd Int. Workshop on Vortex Flows and Related Num. Meth.), vol. 1, 1996, pp. 577–585.
[6] T. Matsushima, P.S. Marcus, A spectral method for unbounded domains, J. Comp. Phys. 137 (1997) 321–345.
[7] J.P. Boyd, Chebyshev and Fourier Spectral Methods, second ed., Dover, Mineola, 2001.
[8] S.K. Stanaway, B.J. Cantwell, P.R. Spalart, Navier–Stokes simulations of axisymetric vortex rings, AIAA Paper 88-0318 (1988).
[9] L. Dufresne, G. Dumas, A 3-D spectral/finite element method for the simulation of the wake vortices hydrodynamic instabilities, CAS J. 44 (4) (1998) 223–230.
[10] L. Dufresne, G. Dumas, A special finite element radial discretization for a Navier–Stokes solver in cylindrical coordinates, in: Proc. 6th Annu. Conf. CFD Soc. Canada CFD98, Québec, 1998, pp. VIII 123–128.
[11] A.G. Kravchenko, P. Moin, R.D. Moser, Zonal embedded grids for numerical simulations of wall-bounded turbulent flows, J. Comp. Phys. 127 (1996) 412–423.
[12] P. Loulou, R.D. Moser, N.N. Mansour, B.J. Cantwell, Direct numerical simulation of incompressible pipe flow using a b-spline spectral method, Technical Memorandum TM-110436, NASA, 1997.
[13] L. Dufresne, A spectral/b-spline method for the navier–stokes equations in unbounded cylindrical coordinates, Ph.D. thesis, Université Laval, Québec, 2001.
[14] C. Canuto, M.Y. Hussaini, A. Quarteroni, T.A. Zang, Spectral Methods in Fluid Dynamics, Springer, New York, 1988.
[15] A. Leonard, Divergence-free vector expansions for 3-D flow simulations, Bull. Am. Phys. Soc. 26 (1981) 1247.
[16] A.J. Chorin, J.E. Marsden, A Mathematical Introduction to Fluid Mechanics, third ed., Texts in Applied Mathematics, vol. 4, Springer, New York, 1993.
[17] R.D. Moser, P. Moin, A. Leonard, A spectral numerical method for the Navier–Stokes equations with applications to Taylor–Couette flow, J. Comp. Phys. 52 (1983) 524–544.
[18] R.D. Moser, P. Moin, Direct numerical simulation of curved turbulent channel flow, Technical Report TF-20, Thermosciences Div., Stanford Univ., 1984.
[19] P.R. Spalart, R.D. Moser, M.M. Rogers, Spectral methods for the Navier–Stokes equations with one or two periodic directions, J. Comp. Phys. 96 (1991) 297–324.
[20] C. de Boor, A Practical Guide to Splines, Springer, New York, 1978.
[21] G.K. Batchelor, Axial flow in trailing line vortices, J. Fluid Mech. 20 (4) (1964) 645–658.
[22] P.G. Drazin, W.H. Reid, Hydrodynamic Stability, Cambridge Univ. Press, New York, 1981.
[23] G.H. Golub, C.F. Van Loan, Matrix Computations, third ed., John Hopkins Univ. Press, Baltimore, 1996.
[24] D.W. Moore, P.G. Saffman, The motion of a vortex filament with axial flow, Philos. Trans. 272 (1972) 403–429.
[25] R.C. Kloosterziel, G.J.F. van Heijst, An experimental study of unstable barotropic vortices in a rotating fluid, J. Fluid Mech. 223 (1991) 1–24.
[26] G.F. Carnavale, R.C. Kloosterziel, Emergence and evolution of triangular vortices, J. Fluid Mech. 259 (1994) 305–331.
[27] R.C. Kloosterziel, G.F. Carnavale, On the evolution and saturation of instabilities of two-dimensional isolated circular vortices, J. Fluid Mech. 388 (1999) 217–257.
[28] S. Houde, G. Dumas, L. Dufresne, Utilisation et avantages d'une approche par zones modales pour un code quasi-spectral en géométrie cylindrique, in: Proc. 8th Annu. Conf. CFD Soc. Canada CFD2K, Montréal, 2000, pp. 57–62.
[29] S.C. Crow, Stability theory for a pair of trailing vortices, AIAA J. 8 (12) (1970) 2172–2178.
[30] T. Leweke, C.H.K. Williamson, Collaborative elliptic instability of a vortex pair, J. Fluid Mech. 360 (1998) 85–119.
[31] F. Laporte, A. Corjon, Direct numerical simulations of the elliptic instability of a vortex pair, Phys. Fluids 12 (5) (2000) 1016–1031.

[32] A.G. Kravchenko, P. Moin, K. Shariff, B-spline method and zonal grids for simulations of complex turbulent flows, J. Comp. Phys. 151 (1999) 757–789.
[33] O. Botella, A high-order approximate-mass spline collocation scheme for incompressible flow simulations, CTR Annu. Res. Briefs, 2000.
[34] O. Botella, On a collocation B-spline method for the solution of the Navier–Stokes equations, Comp. Fluids 31 (2002) 397–420.
[35] W.Y. Kwok, R.D. Moser, J. Jiménez, A critical evaluation of the resolution properties of b-splines and compact finite difference methods, J. Comp. Phys. 174 (2001) 510–551.